

## **Section 6**

Developments in global forecast models, case studies, predictability investigations, global ensembles.



# **Numerical Global Atmospheric Model Findings vis-à-vis International Experiments, I-STEP, INDOEX and GEWEX, relevant to Atmospheric Environment and Global Climate**

**Z.N. Begum**

Ex-Scientist 'G'/Adviser, Department of Science and Technology, New Delhi, India;

OWSD Full Member, ICTP, Trieste, Italy

(Email:begumzn@hotmail.com)

## **Abstract**

This study shows the effect of aerosols and gases on the global energy balance, global environment and climate. Our results provide some insight relevant to global atmospheric models and are in agreement with the findings of the international experiments/programmes, viz., INDOEX, I-STEP and GEWEX.

**Keywords:** Modified AGCM, Atmospheric Environment, Global Climate.

## **1. Introduction**

The interaction of clouds and aerosols plays a major role in the total radiative forcings and vertical distribution of radiative fluxes within the atmosphere. The convective processes provide the mechanism of vertical transport of heat, moisture and momentum, apart from giving rain clouds. It is for this reason that a high priority has been given to cloud-radiation and aerosol radiation interaction studies in some of the International atmospheric research programmes, such as, I-STEP (International Solar-Terrestrial Energy Programme) [1] and INDOEX (Indian Ocean Experiment) [2,3] and GEWEX (Global Energy and Water Cycle Experiment) [4]. Such observations not only improve our understanding of the global experiments, but also help to improve the representation of these processes in the Atmospheric General Circulation Model (AGCM) [5]. We have modified the physical parameterization scheme in the model, which is being referred here as AGCM-M [6-8], where the last alphabet 'M' stands for 'modified'. The modified model has been used to compute the aerosol optical depth and global energy balance.

## **2. Results and discussion**

We have studied the global energy balance computed by using AGCM-M and its comparison with the radiation budget prepared by using the comprehensive radiation budget data collected from the Earth Radiation Budget Experiment (ERBE) (which is a part of I-STEP on global annual mean basis. Due to limitations of space, the data are not presented here. It is found that the present model derived values show similar trend as those reported by Acuha et al. [1], though some slight variation is noticed in the values of some of the parameters.

In Fig. 1 we have plotted the aerosol optical depth computed at 500 nm wavelength using the modified model (AGCM-M) as a function of latitude. It is compared with the INDOEX results obtained by the Indian research vessel Sagar Kanya during 1996-1999 [3,9]. It shows as how much direct sunlight is prevented from reaching the ground by the aerosol particles.

## **3. Conclusion**

These investigations provide some research insight of the model predictions and its role in understanding atmospheric-environmental findings of INDOEX, GEWEX and I-STEP programmes.

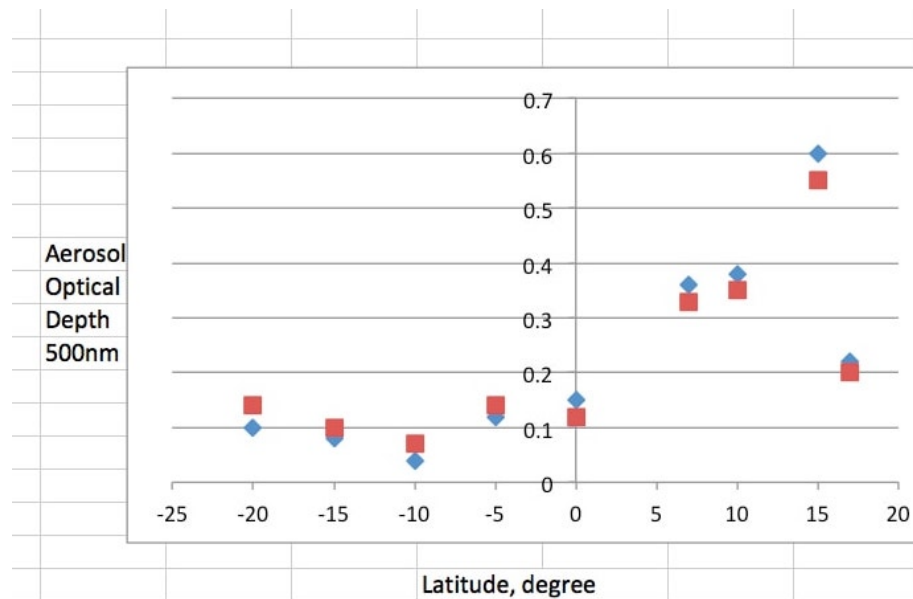


Fig.1. Latitude variation of the aerosol optical depth at 500 nm measured by the Indian Research Vessel 'Sagar Kanya' during 1996 to 1999.

■ INDOEX (Ref. [11]);    ◆ AGCM-M (Present work);

## References

- [1] Acuha, M.H., Ogilvie, K.W., Hoffman, R.A., Fairfield, D.H., Curtis, S.A., Green, J.L., Mish, W.H.: The GGS Science Teams (1997-05-01). "The GGS Program". ISTEP-GGS/SOLARMAX Proposal. Goddard Space Flight Center.
- [2] Gupta, P.K., Sharma, R.C., Koul, S., Parashar, D.C., Mandal, T.K., Mitra, A.P., Study of trace gas species including greenhouse gases over the Indian ocean during INDOEX pre-campaign cruises of 1996, 1997 and 1998 on Sagar Kanya. *Current Science* 1999; 76: 944-946.
- [3] Mitra, A.P., Indian Ocean Experiment (INDOEX): An Overview. *Indian Journal of Marine Sciences* 2004; 33(1): 30-39.
- [4] National Research Council; Division on Earth and Life Studies; Commission on Geosciences, Environment and Resources; Global Energy and Water Cycle Experiment (GEWEX) Panel. Global Energy and Water Cycle Experiment (GEWEX) Continental-Scale International Project: A Review of Progress and Opportunities. 1998. DOI: <https://doi.org/10.17226/6149>.
- [5] Kanamitsu, M., *Weather Forecasting* 1989; 4335-4342.
- [6] Begum, Z.N., Scattering of solar radiation by aerosol particulates in the atmosphere: a theoretical approach validated with Pre-INDOEX. *J. Atmos. Sol. Terr. Phys.* 1998, 60, 1751-4.
- [7] George, J.P., Begum, Z.N., Impact of different radiation transfer parameterization schemes in a GCM on the simulation of the onset phase of Indian Summer monsoon. *Atmosfera* 1997; 10:1-22.
- [8] Begum, Z.N., Investigation of Radiative Effects of Atmospheric and Dust Aerosols Using a Modified Global Spectral Model and Its Impact on the Atmospheric Environment and Climate; In WCRP Report No. 15/2018 (E.Astakhova, Editor). World Climate Research Programme: Research Activities in Atmospheric and Oceanic Modeling, Report No. 48; p. 6-05.
- [9] Jayaraman A., Results on direct radiative forcing of aerosols obtained over tropical Indian Ocean region. *Curr.Sci.* 1999; 76:924-30.

**Cold winters in the North Eurasian regions:  
Risk assessment of El Niño effects**

I.I. Mokhov<sup>1,2</sup>

<sup>1</sup>A.M. Obukhov Institute of Atmospheric Physics RAS

<sup>2</sup>Lomonosov Moscow State University

mokhov@ifaran.ru

The impacts of the El Niño phenomena are significant on a global scale, including North Eurasian regions (Mokhov, Timazhev, 2015; Mokhov, Timazhev, 2016). Here the risk of cold winters, in particular extremely cold winters, in North Eurasian regions is assessed for different El Niño phases. The monthly-mean data for surface air temperature (SAT) anomalies  $\delta T$  in January and February for the period 1936-2014 from (Meshcherskaya and Golod, 2015) for different regions are used. In particular, the ratio of SAT anomalies for January and February to the standard deviation  $\sigma T$  for the period 1961-1990 (index  $\alpha = \delta T / \sigma T$ ) was used for different Russian regions. Winters are ranged for each region as extremely cold winters (ECW), considerably cold winters (CCW) and moderately cold winters (MCW).

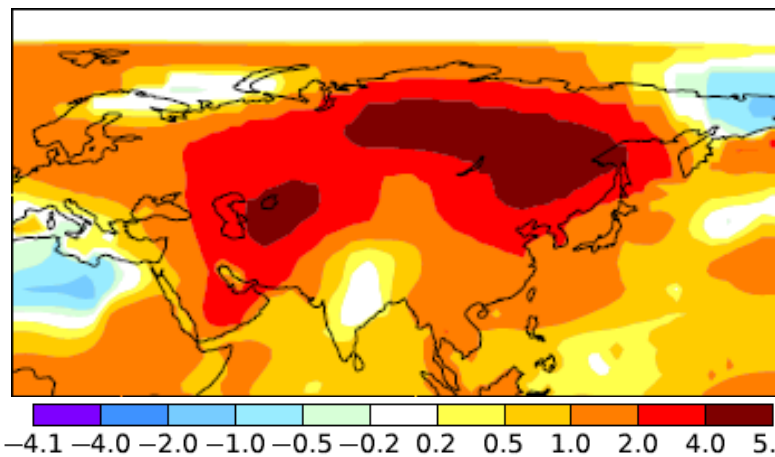


Figure 1. Regional SAT anomalies (K) in January 2019 from GISS data.

Figure 1 shows significant positive SAT anomalies in North Eurasian regions during the El Niño in January 2019 (relative to the period 1951-1980) from GISS data (<https://data.giss.nasa.gov/gistemp/>).

Table 1. Probability of different El Niño phases (characterized by indices Niño3 and Niño4) during 1936-2014.

<b>1936-2014</b>	<i>N</i> $n_N / n_\Sigma$	<i>E</i> $n_E / n_\Sigma$	<i>L</i> $n_L / n_\Sigma$
<b>Niño3</b>	<b>44/79 (0.56)</b>	<b>16/79 (0.20)</b>	<b>19/79 (0.24)</b>
<b>Niño4</b>	<b>40/79 (0.51)</b>	<b>21/79 (0.27)</b>	<b>18/79 (0.23)</b>

Table 1 presents estimates for probabilities ( $n_E/n_\Sigma$ ,  $n_N/n_\Sigma$ ,  $n_L/n_\Sigma$ ) of years starting with El Niño ( $E$ ,  $n_E$ ), La Niña ( $L$ ,  $n_L$ ) or neutral ( $N$ ,  $n_N$ ) phase of ENSO processes detected with the use different indices (Nino3 and Nino4) for the period 1936-2014 ( $n_\Sigma=79$  years).

Table 2. Probability of extremely cold winters (ECW), considerably cold winters (CCW) and moderately cold winters (MCW) in three North Eurasian regions to the south from 60°N in different phases of El Nino, characterized by indices Nino3 and Nino4.

1936-2014		European region			Baikal Lake region			Amur River region		
		ECW	CCW	MCW	ECW	CCW	MCW	ECW	CCW	MCW
Nino3	<i>N</i>	5/8 <b>(0.63)</b>	6/11 (0.55)	8/15 (0.53)	5/8 <b>(0.63)</b>	6/11 (0.55)	11/23 (0.48)	4/8 (0.50)	7/11 <b>(0.64)</b>	11/20 (0.55)
	<i>L</i>	3/8 <b>(0.38)</b>	4/11 <b>(0.36)</b>	3/15 (0.20)	3/8 <b>(0.38)</b>	5/11 <b>(0.45)</b>	8/23 <b>(0.35)</b>	1/8 (0.13)	2/11 (0.18)	5/20 <b>(0.25)</b>
	<i>E</i>	0/8 (0)	1/11 (0.09)	4/15 <b>(0.27)</b>	0/8 (0)	0/11 (0)	4/23 (0.17)	3/8 <b>(0.38)</b>	2/11 (0.18)	4/20 (0.20)
Nino4	<i>N</i>	3/8 (0.38)	6/11 <b>(0.55)</b>	10/15 <b>(0.67)</b>	7/8 <b>(0.88)</b>	6/11 <b>(0.55)</b>	11/23 (0.48)	2/8 (0.25)	8/11 <b>(0.73)</b>	13/20 <b>(0.65)</b>
	<i>L</i>	3/8 <b>(0.38)</b>	4/11 <b>(0.36)</b>	2/15 (0.13)	1/8 (0.13)	5/11 <b>(0.45)</b>	6/23 <b>(0.26)</b>	2/8 <b>(0.25)</b>	1/11 (0.09)	4/20 (0.20)
	<i>E</i>	2/8 (0.25)	1/11 (0.09)	3/15 (0.20)	0/8 (0)	0/11 (0)	6/23 (0.26)	4/8 <b>(0.50)</b>	2/11 (0.18)	3/20 (0.15)

Table 2 shows estimates for probabilities of extremely cold winters (ECW), considerably cold winters (CCW) and moderately cold winters (MCW) in three North Eurasian regions to the south from 60°N in different phases El Nino, characterized by indices Nino3 and Nino4. Probability larger than probability of corresponding El Nino phase are noted in bold. According to Table 2 there is a small probability of ECW and CCW in years starting in *E*-phase in the Baikal Lake region and also in the European region. Quite different risks of cold winters are estimated for the Amur River basin on Far East. The ECW probability for this region in the *E*-phase is quite high. In the European region the probability of ECW and CCW is quite high in the *L*-phase.

This work was supported by the RSF (project No. 19-17-00240). The results obtained in the framework of the RAS Presidium program "Climate change: causes, risks, consequences, problems of adaptation and regulation" and RFBR (projects No. 17-05-01097 and No. 17-29-05098) were used.

## References

- Mescherskaya A.V., Golod M.P. Catalogs of abnormal winters over the Russian territory. Proc. MGO, 2015, **579**, 130–162. (in Russian)
- Mokhov I.I., Timazhev A.V. Drought risk in the North Eurasian regions: Assessment of El-Nino effects. *Res. Activ. Atmos. Ocean. Model.* E. Astakhova (ed.). WCRP Rep. No.12/2015, 2015, 2.6–2.7.
- Mokhov I.I., Timazhev A.V. Weather-climate anomalies in Russian regions: El Niño-associated predictability. *Res. Activ. Atmos. Ocean. Model.* E. Astakhova (ed.). WCRP Rep. No.15/2016, 2016, 6.9–6.10.

## Phase transitions for different El Niño types and periods

Mokhov I.I.<sup>1,2</sup>, Timazhev A.V.<sup>1</sup>

<sup>1</sup> A.M. Obukhov Institute of Atmospheric Physics RAS

<sup>2</sup> Lomonosov Moscow State University

mokhov@ifaran.ru, timazhev@ifaran.ru

The most significant contribution to the interannual variability of the global surface air temperature is associated with the El Niño/Southern Oscillation (ENSO) effects. Here, changes in phase transitions for different El Niño types and periods are estimated. Various phase transitions for different ENSO types were characterized by the Niño3, Niño3.4 and Niño4 indices for different periods during 1891-2015.

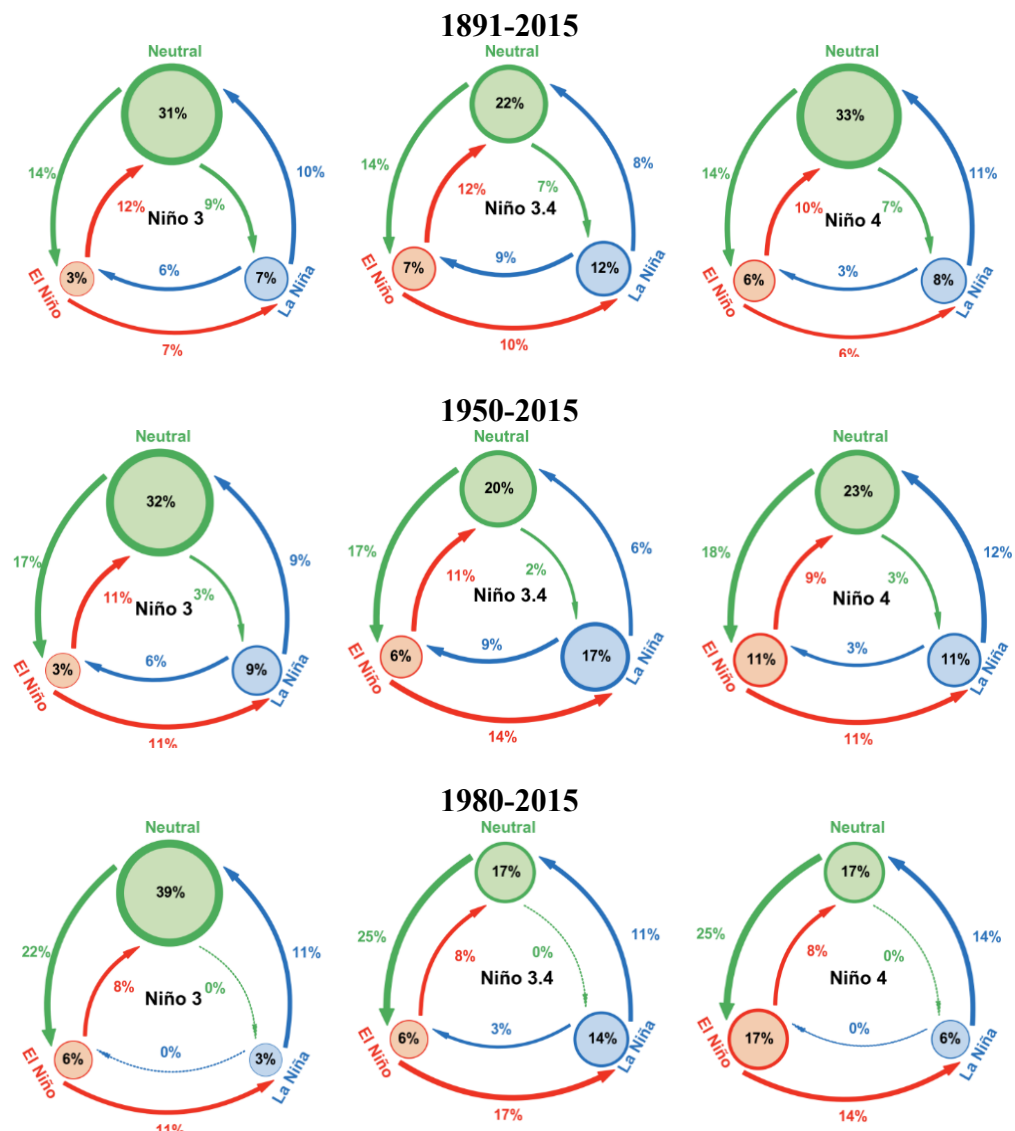


Fig. 1. Estimates of probability for different ENSO phase transitions characterized by various ENSO indices (Niño3, Niño3.4, Niño4) for different periods during 1891-2015.

For estimation of the El Niño/La Niña effects, we used their indices characterized by the sea surface temperature (SST) in the Niño3 (150–90W, 4N–4S), Niño3.4 (170–120°W, 4N–4S) and Niño4 (160E–150W, 4N–4S) regions in the equatorial latitudes of the Pacific Ocean

(<ftp://www.coaps.fsu.edu/>). The El Niño ( $E$ ) and La Niña ( $L$ ) phases were distinguished using 5-month moving averaging of the SST anomaly in the Niño3 region (JMA index). El Niño (warm) and La Niña (cold) phases were defined by the index values of at least 0.5K and at most  $-0.5K$ , respectively, over six consecutive months (including October–December). All the other cases were characterized as neutral phases ( $N$ ).

Nine possible phases of transitions for ENSO are analyzed, including  $N \rightarrow E$  as a transition from the neutral phase in the beginning of the year (winter in the Northern Hemisphere) to the El Niño phase at the beginning of the next year,  $N \rightarrow L$  as a transition from neutral to La Niña phase, and  $N \rightarrow N$  as a prolongation of the neutral phase [1-5]. The number of years ( $n$ ) starting from the neutral phase is about half the total number of the analyzed years ( $n=125$ ). The number of years started from the El Niño and La Niña phases is about a quarter of the total number of the analyzed years.

Figure 1 presents the probability estimates for various ENSO phase transitions characterized by the Niño3, Niño3.4 and Niño4 indices for different periods during 1891-2015: 1891-2015, 1950-2015 and 1980-2015. According to Fig. 1 the phase transition statistics for ENSO differs significantly when using various indices and for different periods. If indices Niño3 and Niño4 are used to classify the transitions, then the number of years beginning from phase  $N$  for the period 1891–2015 ( $n_{\Sigma}=125$ ) is equal to  $n_N=68$ , whereas in the case of using the Niño3.4 index, this number is equal to  $n_N=53$ . The number of years beginning in phases  $E$  and  $L$  is less than a quarter of all years ( $n_{\Sigma}=125$ ):  $n_E(L)=28$  or  $n_E(L)=29$ , depending on the index used (Niño3 or Niño4). In the case of using the Niño3.4 index, the number of years beginning with phases  $E$  and  $L$  ( $n_E(L)=36$ ) is noticeably more - about a third of all years.

The most frequent are the  $N \rightarrow N$  transitions. For ENSO processes detected using the Niño3 index, which characterizes the canonical El Niño with anomalously high SST in the equatorial latitudes of the eastern Pacific Ocean, the  $E \rightarrow E$  transitions are most rare. At the same time, they manifest themselves twice as often in the case of using the Niño 4 index, which characterizes the El Niño regime in the equatorial latitudes of the central part of the Pacific Ocean. When ENSO processes are detected by the Niño4 index, the  $L \rightarrow E$  transitions are the most rare, which are almost twice as often with the Niño3 index.

There are significant differences in phase transitions for different El-Niño types with a significant changes for different time intervals.

This work has been supported by the RSF (project No. 19-17-00240) using the results obtained in the framework of the RAS Presidium program "Climate change: causes, risks, consequences, problems of adaptation and regulation" and RFBR (projects No. 17-05-01097 and No. 17-29-05098).

## References

1. Mokhov I.I., Timazhev A.V. Climatic anomalies in Eurasia from El Niño/La-Niña effects. *Doklady Earth Sci.*, 2013, **453**(1), 1141–1144.
2. Mokhov I.I., Timazhev A.V. Assessment of the predictability of climate anomalies in connection with El Niño phenomena. *Doklady Earth Sci.*, 2015, **464** (2), 1089–1093.
3. Mokhov I.I., Timazhev A.V. Weather-climate anomalies in Russian Regions: El Niño-associated predictability. In: *Research Activities in Atmospheric and Oceanic Modelling*, ed. E. Astakhova, 2016, WCRP Rep. 15/2016, 6.09-6.10.
4. Mokhov I.I., Timazhev A.V. Assessing the probability of El Niño-related weather and climate anomalies in Russian regions. *Russ. Meteorol. Hydrol.*, 2017, **42** (10), 635–643.
5. Mokhov I.I. and Timazhev A.V. Predictability of weather-climate anomalies in the North Eurasian regions during transitions from the La Niña conditions. In: *Research Activities in Atmospheric and Oceanic Modelling*, ed. E. Astakhova, 2018, WCRP Rep. 15/2018, 6.09-6.10.

## Predictability of weather-climate anomalies in the North Eurasian regions for different ENSO transitions during last decades

I.I. Mokhov<sup>1,2</sup> and A.V. Timazhev<sup>1</sup>

<sup>1</sup>A.M. Obukhov Institute of Atmospheric Physics RAS

<sup>2</sup>Lomonosov Moscow State University  
mokhov@ifaran.ru, timazhev@ifaran.ru

The impact of the El Niño / Southern Oscillation (ENSO) processes is significant on a global scale, including North Eurasian regions (Mokhov, Timazhev, 2015, 2016, 2018). In (Mokhov, Timazhev, 2016) estimates of possible anomalies in Russian regions in May-July, 2016 are obtained, taking into account the El Niño phase corresponding to the beginning of the year and its forecasted transformation by the end of the year. Here we analyze observations only for the last decades (since 1980) and present estimates for the predictability of regional climate anomalies in 2019, which begins during the El Niño phase (with positive anomalies of sea surface temperature, SST, in equatorial regions of the Pacific Ocean). According to early-April CPC/IRI official probabilistic ENSO forecast on the basis of ensemble model simulations the probability of the El Niño (*E*) phase continuation to the end of 2019 is about 50%. The corresponding probabilities for neutral (*N*) phase and La Niña (*L*) phase to the end of 2019 are about 40% and 10%, correspondingly.

We analyzed the spring-summer (May-July) anomalies of surface air temperature (SAT)  $\delta T$  and precipitation  $\delta P$ , and also drought (*D*) and excessive moisture (*M*) indices for European (ER) and Asian (AR) parts of Russia in mid-latitudes from observations for the period 1980-2015 according to extended data from (Meshcherskaya et al., 2011). We used different indices of the El Niño / La Niña effects characterized by the sea surface temperature (SST) in the Niño3 and Niño4 regions in the equatorial latitudes of the Pacific Ocean. The El Niño (*E*), La Niña (*L*) and neutral (*N*) phases are defined similar to (Mokhov, Timazhev, 2015, 2016, 2018).

Table 1. Probability of positive and negative surface air temperature anomalies ( $\delta T$ ) in the ER (and AR) in May-July for different ENSO phase transitions (characterized by the Niño3 index) from observations since 1980 for ER and AR (in brackets).

$\delta T, K$		Neutral phase (N) at the beginning of the year			El-Niño phase (E) at the beginning of the year			La-Niña phase at the beginning of the year		
		<i>n</i> =22			<i>n</i> =9			<i>n</i> =5		
Niño3		<i>N</i> → <i>E</i> <i>n</i> =8	<i>N</i> → <i>L</i> <i>n</i> =0	<i>N</i> → <i>N</i> <i>n</i> =14	<i>E</i> → <i>E</i> <i>n</i> =2	<i>E</i> → <i>L</i> <i>n</i> =4	<i>E</i> → <i>N</i> <i>n</i> =3	<i>L</i> → <i>E</i> <i>n</i> =0	<i>L</i> → <i>L</i> <i>n</i> =1	<i>L</i> → <i>N</i> <i>n</i> =4
$>0$	$>0$	6/8 (4/8)	0/0 (0/0)	8/14 (11/14)	2/2 (2/2)	4/4 (3/4)	1/3 (2/3)	0/0 (0/0)	1/1 (1/1)	2/4 (4/4)
	$>1K$	3/8 (3/8)	0/0 (0/0)	6/14 (7/14)	1/2 (2/2)	4/4 (1/4)	0/3 (1/3)	0/0 (0/0)	0/1 (1/1)	2/4 (2/4)
$\leq 0$	$\leq 0$	2/8 (4/8)	0/0 (0/0)	6/14 (3/14)	0/2 (0/2)	0/4 (1/4)	2/3 (1/3)	0/0 (0/0)	0/1 (0/1)	2/4 (0/4)
	$\leq -1K$	1/8 (1/8)	0/0 (0/0)	2/14 (1/14)	0/2 (0/2)	0/4 (0/4)	1/3 (0/3)	0/0 (0/0)	0/1 (0/1)	0/4 (0/4)

Tables 1,2 show the estimates for probability of spring–summer temperature anomalies  $\delta T$  in the ER for different ENSO with the use different index in the Niño3 and Niño4 regions in the equatorial latitudes of the Pacific Ocean. According to Tables 1,2 for the more probable  $E \rightarrow E$  transition in 2019 there is a high probability for extreme positive temperature anomaly  $\delta T$  in May–July for AR. For the less probable  $E \rightarrow N$  transition in 2019 there is a relatively small probability for extreme temperature anomalies for ER and AR in May–July (especially for extreme negative temperature anomalies for AR). For the least probable  $E \rightarrow L$  transition in 2019 there is a large probability for extreme positive temperature anomalies for ER in May–July.

Table 2. Probability of positive and negative surface air temperature anomalies ( $\delta T$ ) in the ER (and AR) in May–July for different ENSO phase transitions (characterized by the Niño4 index) from observations since 1980 for ER and AR (in brackets).

$\delta T$ , K		Neutral phase (N) at the beginning of the year <i>n</i> =15			El-Niño phase (E) at the beginning of the year <i>n</i> =14			La-Niña phase at the beginning of the year <i>n</i> =7		
		<i>N</i> → <i>E</i> <i>n</i> =9	<i>N</i> → <i>L</i> <i>n</i> =0	<i>N</i> → <i>N</i> <i>n</i> =6	<i>E</i> → <i>E</i> <i>n</i> =6	<i>E</i> → <i>L</i> <i>n</i> =5	<i>E</i> → <i>N</i> <i>n</i> =3	<i>L</i> → <i>E</i> <i>n</i> =0	<i>L</i> → <i>L</i> <i>n</i> =2	<i>L</i> → <i>N</i> <i>n</i> =5
>0	>0	5/9 (5/9)	0/0 (0/0)	5/6 (5/6)	3/6 (6/6)	5/5 (4/5)	2/3 (2/3)	0/0 (0/0)	2/2 (1/2)	2/5 (4/5)
	>1K	2/9 (3/9)	0/0 (0/0)	4/6 (3/6)	2/6 (6/6)	4/5 (1/5)	1/3 (1/3)	0/0 (0/0)	1/2 (1/2)	2/5 (2/5)
≤0	≤0	4/9 (4/9)	0/0 (0/0)	1/6 (1/6)	3/6 (0/6)	0/5 (1/5)	1/3 (1/3)	0/0 (0/0)	0/2 (1/2)	3/5 (1/5)
	≤-1K	2/9 (1/9)	0/0 (0/0)	0/6 (0/6)	1/6 (0/6)	0/5 (0/5)	1/3 (0/3)	0/0 (0/0)	0/2 (0/2)	0/5 (1/5)

This work has been supported by the RSF (project No. 19-17-00240). The results obtained in the framework of the RAS Presidium program "Climate change: causes, risks, consequences, problems of adaptation and regulation" and RFBR (projects No. 17-05-01097 and No. 17-29-05098) were used.

## References

- Meshcherskaya A.V., Mirvis V.M., Golod M.P. The drought in 2010 against the background of multiannual changes in aridity in the major grain-producing regions of the European part of Russia. *Tr. MGO*, 2011, **563**, 94–121 (in Russian)
- Mokhov I.I., Timazhev A.V. Drought risk in the North Eurasian regions: Assessment of El-Niño effects. *Res. Activ. Atmos. Ocean. Modell.* E. Astakhova (ed.). WCRP Rep. No.12/2015, 2015, 2.6–2.7.
- Mokhov I.I., Timazhev A.V. Weather-climate anomalies in Russian regions: El Niño-associated predictability. *Res. Activ. Atmos. Ocean. Modell.* E. Astakhova (ed.). WCRP Rep. No.15/2016, 2016, 6.9–6.10.
- Mokhov I.I., Timazhev A.V. Predictability of weather-climate anomalies in the North Eurasian regions during transitions from the La Niña conditions. *Res. Activ. Atmos. Ocean. Modell.* E. Astakhova (ed.). WCRP Rep. No.15/2018, 2018, 6.09–6.10.

# Upgrade of initial perturbations made using the Local Ensemble Transform Kalman Filter in JMA's Global EPS

Yoichiro Ota, Masaaki Ikegami and Haruki Yamaguchi  
(Numerical Prediction Division, Japan Meteorological Agency)  
e-mail: ota@met.kishou.go.jp

## 1. Introduction

The Japan Meteorological Agency (JMA) upgraded its Global Ensemble Prediction System (Global EPS) starting from 00 UTC of March 5, 2019. Modifications from the previous operational version include (1) usage of perturbations from the six-hour forecast ensemble based on the Local Ensemble Transform Kalman Filter (LETKF) of the previous analysis instead of analysis perturbations, and (2) tuning of the horizontal and vertical localization functions in the LETKF. Retrospective experiments covering periods exceeding three months in each of summer 2016 and winter 2016/17 showed an almost-neutral impact as compared to the previous operational version. Exceptions were an increase in spread, especially in the Northern Hemisphere extra-tropics, and a slight improvement in skill for the probability of Tropical Cyclone (TC) strikes in the Northwestern Pacific.

Section 2 briefly outlines the changes included in this upgrade, and Section 3 provides a summary of verification results from retrospective experiments.

## 2. Changes

### (1) Usage of six-hour forecast perturbations from the previous LETKF analysis ensemble

In the previous operational Global EPS, production of atmospheric initial perturbations involved a combination of leading singular vectors (SVs) and analysis perturbations of the LETKF valid at the initial time. The new Global EPS incorporates six-hour forecast perturbations from the previous LETKF analysis ensemble valid at the initial time instead of analysis perturbation. The main objectives of this change are to improve dynamical balance in initial perturbations and enable greater flexibility in operational time schedules.

### (2) Tuning of horizontal and vertical localization functions in the LETKF

The horizontal localization length scale (in which the localization function is the inverse square root of  $e$ ) of humidity-sensitive observations was shortened from 400 to 300 km based on the diagnostics of Ménétrier et al. (2015). The vertical localization function of satellite radiance observations was also changed from a normalized weighting function to the maximum of the normalized weighting function and Gaussian function with a length scale of 0.8 for scale heights centered at the peak of the weighting function.

## 3. Retrospective experiment results

A set of retrospective experiments was performed before approval of the upgrade for implementation in the operational system. The experimental periods covered 00 and 12 UTC initials from June 20 2016 to October 11 2016 (summer) and from November 20 2016 to March 11, 2017 (winter). In addition, all four initials (00, 06, 12 and 18 UTC) from 2016 to 2018 for periods when any TCs were present in the Northwestern Pacific were covered for verification of TC track forecasts. Two experiments were performed with the previous (CNTL) and new (TEST) versions of the Global EPS.

Figure 1 compares the spread of 500-hPa geopotential heights [m] in the Northern Hemisphere extra-tropics (20 – 90°N) in the summer experiment. The spread increased in forecasts with lead times up to nine days, thereby improving the spread-skill relationship of medium-range forecasts (i.e., those with lead times of five days or more; not shown). Figure 2 shows an example involving ensemble track forecasts for Typhoon Mangkhut (2018). It can be seen that the new system exhibits a larger spread for central positions of the TC for short-range forecasts in particular. This mitigates the underdispersiveness of TC positions and improves the skill of strike probabilities for TCs in the Northwestern Pacific in forecasts with lead times of up to three days (not shown).

References

Ménétrier B., T. Montmerle, Y. Michel and L. Berre, 2015: Linear filtering of sample covariances for ensemble-based data assimilation. Part I: Optimality criteria and application to variance filtering and covariance localization. *Mon. Wea. Rev.*, **143**, 1,622 – 1,643.

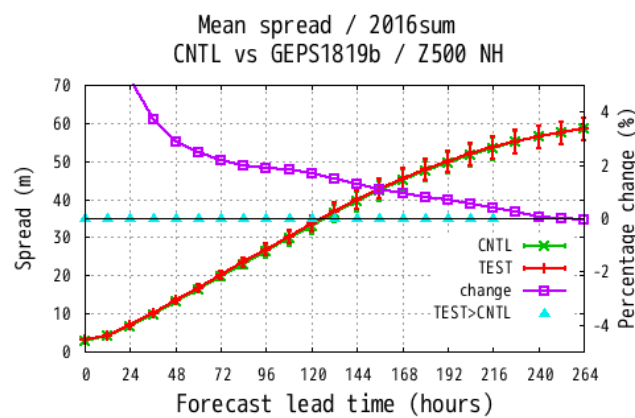


Figure 1 Spread of 500-hPa geopotential height [m] in the Northern Hemisphere extra-tropics (20 – 90°N) in the summer experiment. The horizontal axis shows the forecast lead time in hours, and the green and red lines show the spread (left axis) of CNTL and TEST, respectively. The purple line shows the normalized change of the spread [%] (right axis). The light-blue triangles indicate that increases of the spread in TEST are statistically significant with 95% confidence based on the bootstrap method.

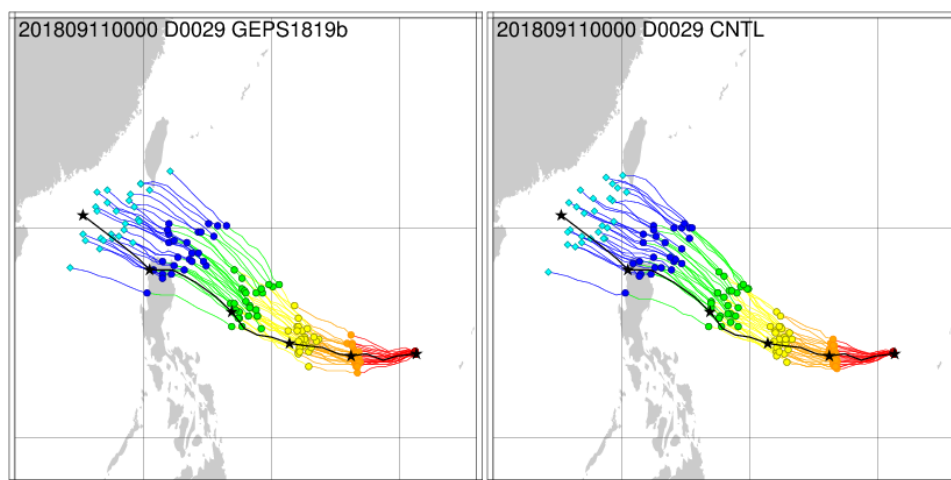


Figure 2 Central position forecasts for Typhoon Mangkhut (2018) at 00 UTC on September 11 2018 (initial) for TEST (left) and CNTL (right). The black line follows best-track analysis positions produced by RSMC/Tokyo. Red, orange, yellow, green, dark-blue and light-blue markers show TC central positions in forecasts with lead times of 0, 1, 2, 3, 4 and 5 days, respectively.

# Interactions between GFDL Cloud Microphysics and RRTMG Radiation in NCEP FV3GFS

Ruiyu Sun<sup>1,3</sup>, Bing Fu<sup>1,3</sup>, Jongil Han<sup>3,4</sup>, Yu-tai Hou<sup>3</sup>, Shian-Jiann Lin<sup>2</sup>, Jun Wang<sup>3</sup>,  
Fanglin Yang<sup>3</sup>, Linjiong Zhou<sup>2,5</sup>, Xiaoqiong Zhou<sup>1,3</sup>

1. IMSG, Inc., 2. GFDL/NOAA, 3. EMC/NCEP/NOAA,  
4. SRG, and 5. Princeton University  
Email: Ruiyu.Sun@noaa.gov

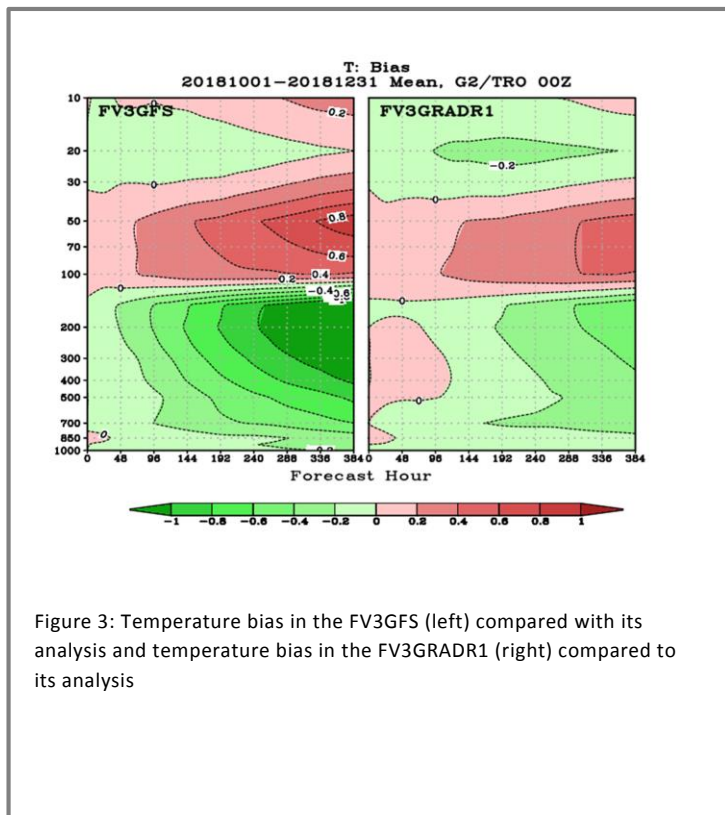
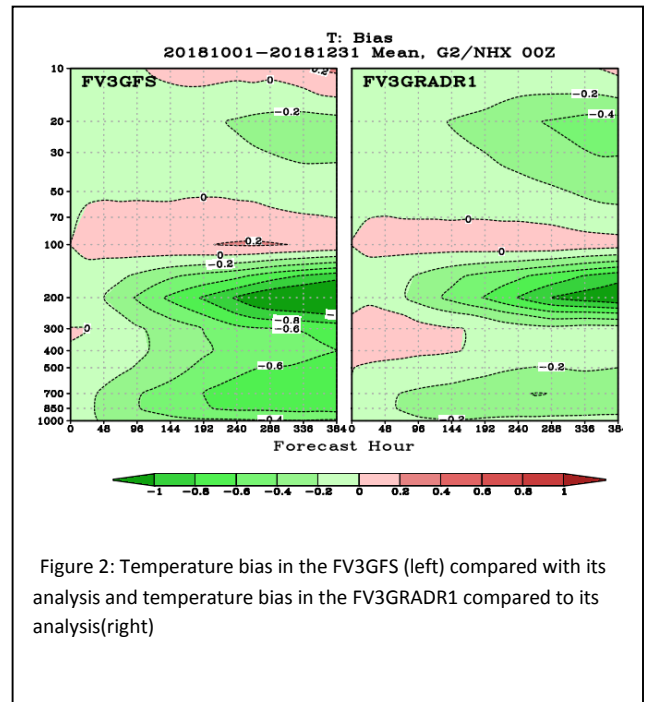
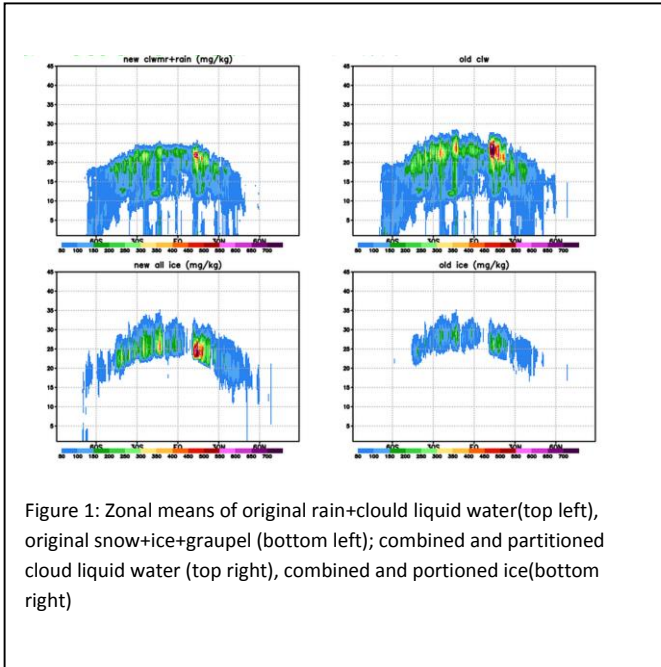
Clouds play a critical role in regulating the radiative transfer through the atmosphere and the energy budget at the surface. Whether a given cloud will heat or cool the atmosphere and the surface depends on several factors, including the cloud's altitude, its size, and the properties of the particles that form the cloud. Cloud properties defined by the RRTMG radiation module implemented in the current NCEP FV3GFS include cloud fraction, contents and particle sizes of cloud liquid water, cloud ice, rain, and snow. In the early implementation of the interaction between the GFDL cloud microphysics scheme and the RRTMG radiation in the FV3GFS, all the cloud hydrometeors are combined and then partitioned into cloud liquid water and cloud ice based on a temperature-dependent empirical function before they are passed to the radiation. The radius of cloud liquid water is a function of temperature and land surface type. The radius of the ice particles is a function of temperature and cloud ice content (Heymsfield and McFarquhar, 1996). One drawback of this approach is that certain types of liquid hydrometeors from the GFDL microphysics might be incorrectly treated as ice, and vice versa, in the radiation. Figure 1 illustrates the effect of this approach on hydrometers seen by the radiation. The top left panel shows the zonal-mean cloud liquid water and rain from cloud microphysics. The top right panel shows the zonal-mean cloud liquid water after the combination and partitioning. There is much more liquid in the latter case, indicating some of the ice has been regrouped into liquid cloud water. To correct this mismatch, a new cloud-radiation interaction scheme between the GFDL cloud microphysics (Zhou et al., 2019) and RRTMG radiation was implemented into the FV3GFS. In the new scheme, the water contents and effective radii of individual cloud hydrometeors from the GFDL cloud microphysics are directly passed into the RRTMG radiation. -- Note that graupel is treated as snow because there is no graupel category in RRTMG.

A fully cycled experiment (named FV3GRADR1) with data assimilation was run for three months to test the new cloud-radiation interaction scheme. The experiment covers the period from October 1<sup>st</sup>, 2018 through December 31<sup>st</sup>, 2018. Results from this experiment were compared to the experiment with the old cloud-radiation interaction scheme (named FV3GFS). Shown in Figure 2 are temperature biases, verified against each experiment's own analysis, in the Northern Hemisphere. The cold bias found in the old experiment is reduced throughout the troposphere in FV3GRADR1, and the warm bias in the lower stratosphere is also reduced. This reduction in bias is also presented in the verification against rawinsonde observations. Temperature biases in the Northern Hemisphere at the 24 and 48 forecast hours are reduced in FV3GRADR1 except at layers from 450 hPa to 200 hPa. RMSE is improved at all layers. A similar improvement is also found in the Southern Hemisphere (figures not shown). In the tropics, temperature RMSE is greatly reduced around 200 hPa (Figure 3). Wind RMSE is reduced in the tropical region. Other noticeable improvements in FV3GRADR1 over FV3GFS include the smaller OLR biases and less prominent 2-meter temperature cold biases over the polar region.

## References

[1] Heymsfield A., and G. M. McFarquhar, 1996: High albedos of cirrus in the tropical Pacific warm pool: Microphysical interpretations from CEPEX and from Kwajalein, Marshall Islands. *J. Atmos. Sci.*, **53**, 2424–2451.

[2] Zhou, L., S.-J. Lin, J.-H. Chen, L.M. Harris, X. Chen, and S.L. Rees, 2019: Toward Convective-Scale Prediction within the Next Generation Global Prediction System. *Bull. Amer. Meteor. Soc.*, <https://doi.org/10.1175/BAMS-D-17-0246.1>, in press.



# Reduction of 2-m Temperature Forecasting Errors in the NCEP Global Forecast System

Weizhong Zheng<sup>1</sup>, Jack Kain<sup>2</sup>, Jongil Han<sup>3</sup>, Shrinivas Moorthi<sup>2</sup>, Ruiyu Sun<sup>1</sup>, Helin Wei<sup>1</sup>, Fanglin Yang<sup>2</sup>

<sup>1</sup>IMSG at NOAA/NCEP/EMC, College Park, MD 20740, USA; <sup>2</sup>NOAA/NCEP/EMC, College Park, MD 20740, USA; <sup>3</sup>SRG@NOAA/NCEP/EMC, College Park, MD20740, USA

Email: Weizhong.Zheng@noaa.gov

## 1. Introduction

Accurate forecast of the near surface fields in numerical models is regarded as the key for improving numerical weather and climate prediction, although it has proven to be challenging. Different types of biases and systematic errors are found in near-surface forecasts. They can be attributed to various factors such as the land surface model, planetary boundary scheme, other physics processes, and coupling between the surface and atmosphere (Mahrt 2014; Steeneveld 2014; Zheng et al. 2017, Haiden et al. 2018). It has long been known that the NOAA National Centers for Environmental Prediction (NCEP) Global Forecast System suffers from large biases in near surface forecasts over land. This study addresses the wintertime 2-m temperature warm bias in the first version of the Finite Volume Cubed Sphere (FV3) dynamic core based GFS (GFSv15). The background diffusivity in the planetary boundary scheme is revealed to strongly modulate the 2-m temperature forecast. Optimization of this parameter shows significant positive impact for cases where large wintertime warm biases exist.

## 2. Methodology

The FV3GFS uses the hybrid eddy-diffusivity mass-flux (EDMF) planetary boundary layer scheme. It includes dissipative heating and modified stable boundary layer mixing (Han et al. 2016). The background diffusivity  $K_0$  for momentum, heat and moisture used in the GFS exponentially decreases with height,

$$K_0 = d_k e^{[-10(1-P/P_s)^2]}, \quad (1)$$

where  $P$  is atmospheric pressure,  $P_s$  is surface pressure, and  $d_k$  is a constant, set to 1.0 in this model.

To investigate how the background diffusivity affects the PBL structure and near-surface parameters, various  $d_k$  or  $K_0$  values are tested. The background diffusivity is further modified based on the stability as follows:

$$\begin{aligned} d'_k &= d_k, \text{ for } R_{ib} \leq 0 \\ d'_k &= d_k \times \left(1 - \frac{R_{ib}}{R_{ibc}}\right)^2 + d_{kmin} \times \left[1 - \left(1 - \frac{R_{ib}}{R_{ibc}}\right)^2\right], \quad \text{for } 0 < R_{ib} < R_{ibc} \\ d'_k &= d_{kmin}, \quad \text{for } R_{ib} \geq R_{ibc} \end{aligned} \quad (2)$$

where  $R_{ib}$  is the surface bulk Richardson number,  $R_{ibc}$  equals to 0.25 and  $d_{kmin}$  equals 0.1. Two values of  $d_k$ , 1.0 and 2.0, are tested in this report.

## 3. Forecast experiments

A case study covering the period December 18 to 23, 2017 was selected. The FV3GFS was integrated forward for 7 days. One control run and three sensitivity experiments were carried out. The control run (CTL) uses the model default value of  $d_k=1$ .  $d_k$  is further set to 0.0, 0.1 and 0.5 in the sensitivity runs KK00, KK1 and KK2. Both KK1 and KK2 use the modified background diffusivity with the stability, while  $d_k$  is set to 1.0 and 2.0, respectively. Figure 1 shows the 2-m temperature change for the 3-h period ending at 0000 UTC December 23, 2017. The control run has a large warm bias, up to 7 °C in the evening, indicating the surface layer is overly mixed. Reduction of the background diffusivity results in cooler 2-m temperatures. In the KK00 run with no background diffusivity, the model 2-m temperature is even lower than the observation at night. Daytime 2-m temperature also decreased, resulting in a large daytime cold bias. The modification of  $K_0$  based on the stability substantially reduced the night-time warm bias, bringing the forecast closer to the observations. The KK2 run also exhibits a weaker daytime cold bias than does the KK1 run.

To gain more insight into the impact of the proposed change on forecast skill, a set of daily 7-day forecasts were conducted for a one-month winter period. Figure 2 presents the changes in 2-m temperature diurnal cycle over the CONUS west between the CTL and KK2 experiments. The CTL run has night-time temperatures warmer than the observed, up to 1.6 degrees. KK2 reduced this warm bias, with reductions up to 0.5 °C.

Figure 3 shows the 500-hPa geopotential height anomaly correlation coefficient. A positive impact from the proposed change is evident for the first 120 hours of the forecast. The improvement is statistically significant at the 95% confidence level.

## 4. Summary

Background diffusivity has a significant impact on 2-m temperature. Results from a set of medium-range forecasts showed that the proposed modification to the background diffusivity reduced the systematic 2-meter temperature warm bias in the FV3GFS. In addition, the 500-hPa height anomaly correlation was improved as well.

## References

- Han, J., M. L. Witek, J. Teixeira, R. Sun, H.-L. Pan, J. K. Fletcher, and C. S. Bretherton, 2016: Implementation in the NCEP GFS of a hybrid eddy-diffusivity mass-flux (EDMF) boundary layer parameterization with dissipative heating and modified stable boundary layer mixing. *Wea.Forecasting*, 31, 341–352, doi:10.1175/WAF-D-15-0053.1.
- Haiden, T, I. Sandu, G. Balsamo, G. Arduini and A. Beljaars, 2018: Addressing biases in near-surface forecasts, *ECMWF Newsletter*, 157, 20-25.
- Marht, L, 2014: Stably stratified atmospheric boundary layers. *Annu. Rev. Fluid Mech.*, 46, 23–45, doi:10.1146/annurev-fluid-010313-141354.
- Steenefeld, G.-J., 2014: Current challenges in understanding and forecasting stable boundary layers over land and ice. *Front. Environ. Sci.*, 2, doi:10.3389/fenvs.2014.00041.
- Zheng, W., Ek, M., Mitchell, K., Wei, H., & Meng, J. (2017). Improving the stable surface layer in the NCEP global forecast system. *Monthly Weather Review*, 145, 3969–3987, <https://doi.org/10.1175/mwr-d-16-0438.1>.

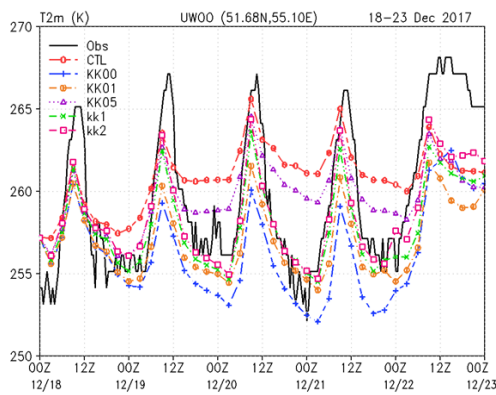


**Fig.1.** 3-hourly 2-m temperature (K) (a) and 10-m wind speed (m/s) (b) at the UWOO station for different  $d_k$  values for December 18 to 22, 2017.

**Fig. 2.** The top panel depicts 2-m temperature diurnal cycle averaged over the CONUS West and for the period of 1–31 December 2017 for observation (black), the CTL run (red) and the KK2 (green), respectively. The bottom panel shows the differences of the experiments compared to the observation. Differences outside of the hollow bars are statistically significant at the 95% confidence level for a Student’s t test.

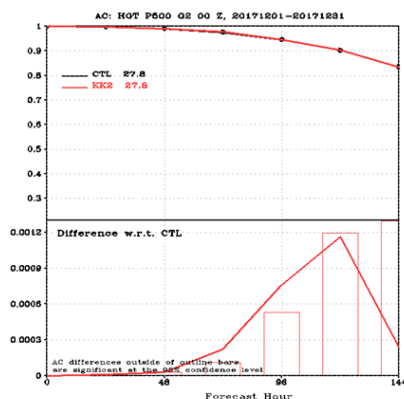
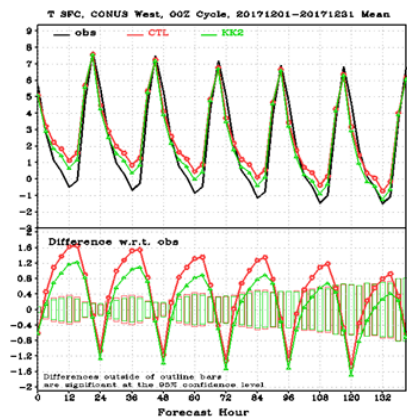


**Fig. 3.** Global mean anomaly correlation coefficient of 500-hPa geopotential heights as a function of forecast length (top panel), and the differences between the KK2 and CTL runs. Differences outside of the hollow bars are statistically significant at the 95% confidence level for a Student’s t test.

# Reduction of Excessive Cold Bias in GFS 2-m Temperature Forecasts in Snow-Free Seasons

Weizhong Zheng<sup>1</sup>, Kenneth Mitchell<sup>3</sup>, Michael Ek<sup>2</sup>, Jack Kain<sup>2</sup>, Helin Wei<sup>1</sup>

<sup>1</sup>IMSG at NOAA/NCEP/EMC, College Park, MD 20740, USA; <sup>2</sup>NOAA/NCEP/EMC, College Park, MD 20740, USA; <sup>3</sup>Prescient Weather Ltd, State College, PA 16803, USA  
Email: Weizhong.Zheng@noaa.gov

## 1. Introduction

Understanding and predicting 2-m surface temperature forecasts over land in numerical models is regarded as both essential and challenging, owing to multiple related physical processes and their complex interactions. It has long been known that the Global Forecast System (GFS) of the National Centers for Environmental Prediction (NCEP) has large errors in the forecast of near-surface air temperature in some regions (e.g., Bosveld et al. 2014). In particular, excessive cold biases of 2-m air temperature are typical in the late afternoon and nighttime, especially during spring, autumn and winter, suggesting the biases are related to the transition from the daytime unstable boundary layer to nocturnal stable conditions.

Zheng et al. (2017) proposed practical approaches to reduce the excessive cooling of surface skin temperature and 2-m air temperature and prevent the collapse of turbulence and potential numerical instability resulting from thermal decoupling of the land surface and atmosphere. The most effective of the three modifications is introducing a constraint on the ( $z/L$ ) stability parameter in the Monin-Obukhov similarity theory. Applying these modifications to the GFS surface layer parameterization (Zheng et al., 2017), this study executes daily GFS 7-day test forecasts for one month in early autumn to determine if GFS 2-m air temperature forecasts are consistently improved during a full month of daily forecasts under snow-free conditions.

## 2. Assessment of daily autumn forecast experiments

Unlike the winter period in Zheng et al. (2017), this early autumn period is virtually snow-free over the entire CONUS land surface (except locally over high mountains). The NCEP operational GFS forecasts presented here illustrate that the excessive GFS cooling of 2-m temperature over land in the late afternoon and nighttime also occurs in snow-free conditions. This phenomenon frequently occurs over much of CONUS as well as Alaska (though part of Alaska is covered by snow during this autumn case).

The impact of the changes on early autumn GFS 2-m temperature forecasts is similar to that in winter, but the error reduction achieved in the sensitivity experiment is less than in winter. Therefore, we examine smaller sub-regions to better see the impact of the changes. Figure 1 presents the areal and temporal mean diurnal cycle (Fig. 1a) and root-mean-square error (RMSE) (Fig. 1b) of the GFS control run (CTL) and experiment (EXP) forecasts of 2-m surface air temperature over the Northwest CONUS, as a function of the model 7-day forecast length. The Northwest subregion is mostly covered in needleleaf evergreen forest with a large roughness length. The CTL exhibits some warm biases in the morning and near noon, but a rather large cold bias in the late afternoon and nighttime, approaching 3.5 °C. The EXP significantly reduces the cold bias, up to 1.5 °C near sunset. The CTL RMSE typically features the largest errors in late afternoon (Fig. 1b). The RMSE reduction in the EXP is quite evident during the 7-day forecast, particularly around 0000 UTC daily, which is a transitional period from daytime unstable to nocturnal stable conditions. It is noteworthy that not only does the EXP RMSE reduction reach 1.2 °C, which amounts to about a 25% reduction of total RMSE versus the CTL, but the daytime RMSE also dropped.

In Figure 2, forecast vertical temperature profiles verified against observed soundings reveal that CTL has a consistent warm bias in the low atmosphere. The excessive surface cooling and associated decoupling arising from the very small, or virtually zero surface sensible heat flux in very stable conditions, results in a counterpart *warm* bias in the lower atmosphere *above* the surface layer. Thus, as in winter, the impact in early autumn is more evident in the colder Northern Hemisphere than the Southern Hemisphere or Tropics. As seen in Figure 2 at the 12-h and 36-h forecast, the reduction of bias and RMSE is obvious in the EXP from the surface up to 850 hPa in the Northern Hemisphere. More notable impacts can be found in the NH sub-regions such as North America, Asia (5 °N - 65 °N and 60 °E - 145 °E) and Europe (30 °N - 70 °N and 10 °W - 45 °E). In North America where the 12-h and 36-h forecasts are in the early morning, the warm bias is reduced to about 0.25 °C in EXP. The EXP reduction of bias and RMSE extends from the surface up to 700 hPa, which is much deeper than the boundary layer. In Asia where the 12-hour and 36-hour forecasts are late afternoon, the CTL also has a warm bias near the surface and this warm bias is again reduced in the EXP. Moreover, in Europe where the 12-hour and 36-hour forecasts are around noon, the impact is also obvious, despite the proposed surface layer changes being oriented toward the stable boundary layer.

Last, the precipitation forecast skill in early autumn over the CONUS shows some improvement in the 12-h

to 36-h forecast range or the 36-h to 60-h forecast range, but is not shown because the skill difference does not attain the 95% confidence level. Unlike in winter, precipitation in the relatively warm late summer and early autumn period of August 15 to September 22 is mainly convective, which is usually initiated during unstable daytime hours, and is much less often associated with stable boundary layer conditions. Therefore, the stable surface layer modifications proposed in this study were not expected to meaningfully impact precipitation forecast skill in late summer and early autumn.

### 3. Summary and ongoing research

A comprehensive set of daily 7-day GFS forecast experiments spanning one-month or longer period in early autumn demonstrated that the proposed approach considerably reduced 2-m temperature cold bias and RMSE in the late afternoon and evening. These model changes also affected levels above the surface layer and obviously reduced the bias and RMSE of atmospheric temperatures in the lower troposphere. No significant impacts are seen in warm-season precipitation forecasts over CONUS, given that the convective precipitation dominating the warm season is mostly associated with daytime unstable boundary layers.

There are still many issues related to coupled land-atmosphere processes and forecasts of near-surface fields. With the first version of FV3 dynamic core based GFS, more studies on the interactive land surface with radiation processes, PBL, clouds, etc., will be performed and further reduction of model forecast errors of near-surface fields is anticipated.

### References

Bosveld, F. C., P. Baas, G. Steeneveld, A. A. M. Holtslag, W. M. Angevine, E. Bazile, E. I. F. de Bruijn, D. Deacu, J. M. Edwards, M. Ek, V. E. Larson, J. E. Pleim, M. Raschendorfer and G. Svensson, 2014: The GABLS third intercomparison case for model evaluation. Part B: SCM model intercomparison and evaluation. *Bound.-Layer Meteor.*, 152, 157-187, doi:10.1007/s10546-014-9919-1.

Zheng, W., Ek, M., Mitchell, K., Wei, H., & Meng, J. (2017). Improving the stable surface layer in the NCEP global forecast system. *Monthly Weather Review*, 145, 3969–3987, <https://doi.org/10.1175/mwr-d-16-0438.1>.

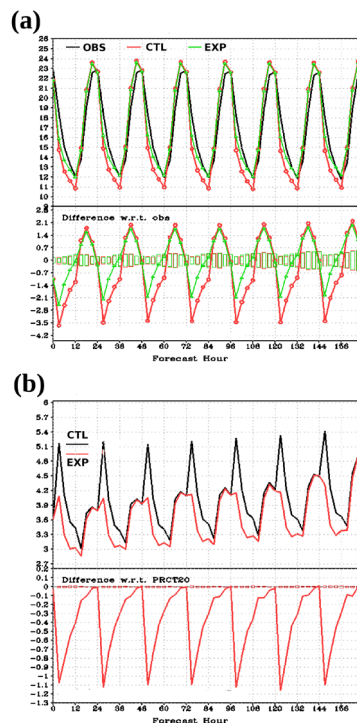


FIG. 1. (a) (top) Mean 7-day diurnal cycle of T2m (°C) averaged both spatially over the northwest CONUS and temporally over the period of 15 Aug–22 Sep 2014, for observations (black), and 7-day GFS forecast from CTL (red) and EXP (green); (bottom) as in (top), but shows difference of CTL (red) and EXP (green) from observations, plus the results of a statistical Student's t test/significance test. The differences outside of the hollow bars attain the 95% confidence level based on the Student's t tests. (b) (top) Corresponding RMSE of CTL (black) and EXP (red) with respect to observations as function of forecast length over 7 days for the same period as in (a); (bottom) difference of CTL and EXP time series in the top plot, plus the results of a statistical Student's t test/significance test. The differences outside of the hollow bars attain the 95% confidence level based on the Student's t tests.

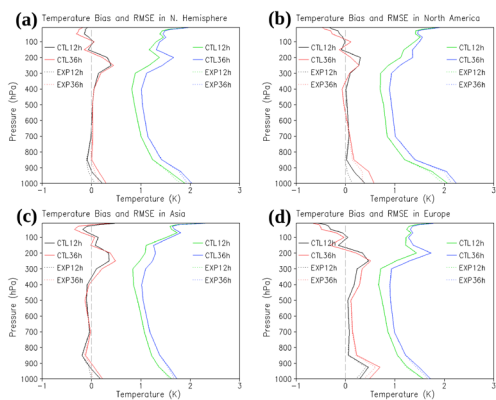


FIG. 2. Mean vertical profiles of air temperature (K) bias and RMSE for CTL (solid) and EXP (dot-dash) forecasts verified against radiosonde observations, as temporally averaged over the period of 15 Aug–22 Sep 2014 and spatially averaged over the (a) Northern Hemisphere, (b) North America, (c) Asia and (d) Europe. Black lines (red lines) are bias from 12-h (36 h) forecasts. Green lines (blue lines) are RMSE from 12-h (36 h) forecasts.